

Ferroelectric Single-Molecule Magnet with Toroidal Magnetic Moments

Yu-Xia Wang, Yinina Ma, Jie-Su Wang, Yue Yang, Yun-Nan Guo, Yi-Quan Zhang,*
Kui-Juan Jin, Young Sun,* and Peng Cheng*

Materials that coexist magnetic and electric properties on the molecular scale in single-molecule magnets (SMMs) with peculiar quantum behaviors have promise in molecular electronics and spintronics. Nevertheless, such molecular materials are limited in potentials because their magnetic signal cannot be transformed into an electrical signal through magnetoresistance or Hall effects for their high insulativity. The discovery of an entirely new material, ferroelectric SMMs (FE SMMs) is reported. This FE SMM also shows single-molecule magnetic behaviors, toroidal magnetic moments, and room-temperature ferroelectricity. The toroidal moment is formed by a vortex distribution of magnetic dipoles in triangular Dy₃ clusters. The analysis of ac magnetic susceptibility reveals the coexistence of three distinct magnetic relaxation processes at low temperatures. The ferroelectricity is introduced by incorporating polar alcohol molecules in the structure, which is confirmed by the X-ray diffraction and optical second harmonic generation (SHG) measurements. Moreover, the dielectric measurements reveal a ferroelectric-to-ferroelectric phase transition around 150 K due to the symmetry change from *Pc* to *Pna2₁*. The coexistence of toroidal moment and ferroelectricity along with quantum magnetism in the rare-earth single-molecule magnets yields a unique class of multiferroics.

1. Introduction

Single-molecule magnets (SMMs) are discrete molecular species with quantum tunneling behaviors of magnetism.^[1] Many SMMs with different structures and magnetic ions have been designed and synthesized in the past two decades.^[2–5] Recently, SMMs with fantastic toroidal moments have attracted much attention owing to their special spin arrangement and abundant quantum magnetism,^[6] where the toroidal moment is characterized by a vortex distribution of magnetic dipoles.^[7] The toroidal moment is regarded as an electromagnetic moment in addition to traditional electric polarization and magnetization,^[8] and the concept of multiferroics has been extended to include the ferro-toroidal order.^[9] A lot of intriguing properties based on toroidal moments have been observed in recent years.^[10–14]

Although the magnetic properties of SMMs have been extensively studied, their

Y.-X. Wang, Y. Yang, P. Cheng
Key Laboratory of Advanced Energy Materials Chemistry (MOE)
Haihe Laboratory of Sustainable Chemical Transformations (Tianjin)
Renewable Energy Conversion and Storage Center
College of Chemistry
Nankai University
Tianjin 300071, P. R. China
E-mail: pcheng@nankai.edu.cn
Y. Ma, K.-J. Jin
Institute of Physics
Chinese Academy of Sciences
Beijing 100190, P. R. China

J.-S. Wang
Division of Quantum States of Matter
Beijing Academy of Quantum Information Sciences
Beijing 100193, China
Y.-N. Guo
Department of Chemistry
Zhejiang Sci-Tech University
Hangzhou 310018, P. R. China
Y.-Q. Zhang
Jiangsu Key Lab for NSLSCS
School of Physical Science and Technology
Nanjing Normal University
Nanjing 210023, P. R. China
E-mail: zhangyiquan@njnu.edu.cn

Y. Sun
Center of Quantum Materials and Devices and Department of Applied
Physics
Chongqing University
Chongqing 401331, P. R. China
E-mail: youngsun@cqu.edu.cn

 The ORCID identification number(s) for the author(s) of this article can be found under <https://doi.org/10.1002/advs.202202979>

© 2022 The Authors. Advanced Science published by Wiley-VCH GmbH. This is an open access article under the terms of the Creative Commons Attribution License, which permits use, distribution and reproduction in any medium, provided the original work is properly cited.

DOI: 10.1002/advs.202202979

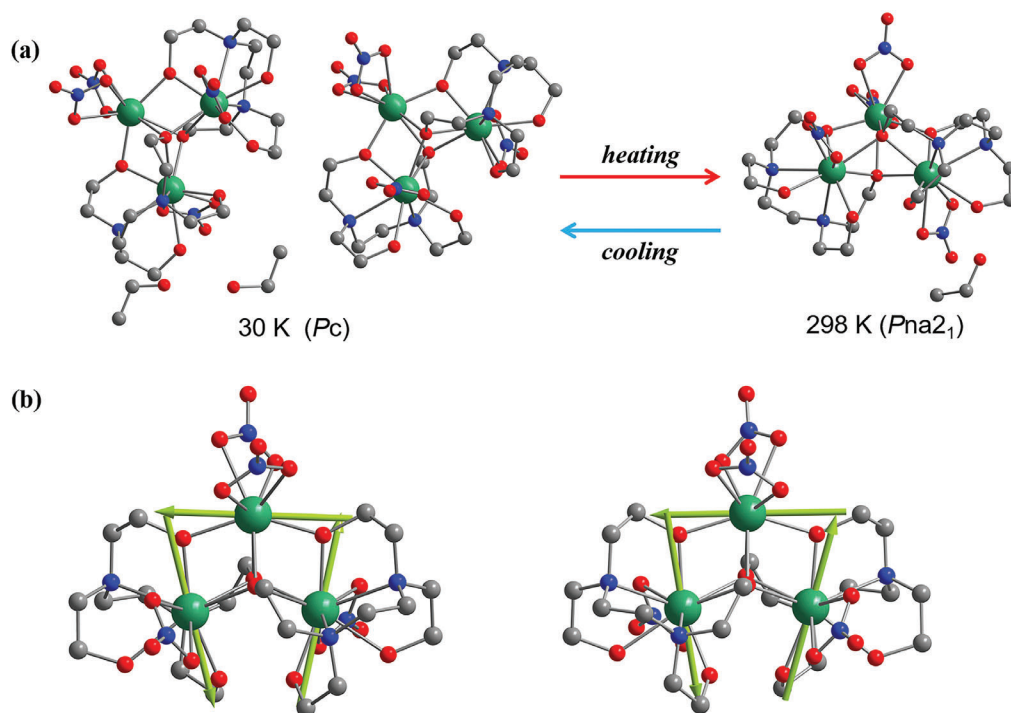


Figure 1. Crystalline structure and toroidal magnetic moments. a) Crystal structure and space group at 298 and 30 K. b) Toroidal magnetic moments in two configurations of Dy₃ clusters at low temperatures. The arrows represent the calculated orientations of the local magnetic easy axes on Dy³⁺ ions. Color scheme: green Dy, red O, grey C, and blue N. The hydrogen atoms and the isopropanol molecules are omitted for clarity.

electric properties have been less concerned because they are generally insulating dielectrics without magnetoresistance or Hall effects. This feature makes SMMs unfavorable for applications in electronic and spintronic devices.^[15,16] However, when ferroelectricity is introduced into SMMs, their functionality would be greatly expanded in terms of multiferroicity and magnetoelectric effects. In fact, there has been growing interest in achieving ferroelectricity in organic molecular materials and metal-organic frameworks beyond traditional ferroelectric oxides.^[17–19] Nevertheless, ferroelectricity in SMMs has not been convincingly achieved. In this letter, we report the discovery of ferroelectricity above room temperature in a peculiar SMM with toroidal magnetic moments.

In this work, we constructed and characterized the solid evidences of SMM and ferroelectricity in a ferroelectric SMM,^[20] [Dy₃(HL)(H₂L)(NO₃)₄]·C₂H₅OH (H₄L = *N,N,N',N'*-tetrakis(2-hydroxyethyl)-ethylene-diamine), which possesses toroidal moment formed by a vortex distribution of magnetic dipoles in triangular Dy₃ clusters. Interestingly, we find three-step magnetic relaxation processes coexisting in the same temperature range. A modified Debye model with three relaxation times was introduced to study the multiple dynamic mechanisms as well. The ferroelectricity with the Curie temperatures $T_C \approx 470$ K was evidenced by the SHG signal that is only allowed in non-centrosymmetric structures. Moreover, the dielectric anomaly around 160–170 K suggests a ferroelectric-to-ferroelectric phase transition originated from the structural transformation from *Pc* to *Pna*₂₁.

2. Results and Discussion

X-ray diffraction studies reveal that the SMM crystallizes in the polar space group *Pna*₂₁ at 298 K (Figure 1a). There are three crystallography-independent Dy³⁺ ions and one alcohol molecule in the polar *Pna*₂₁ space group. One eight-coordinated Dy³⁺ ion (Dy1) is coordinated by eight oxygen atoms (DyO₈) from two nitrates and two ligands, while the other two nine-coordinated Dy³⁺ ions (Dy2 and Dy3) are surrounded by two nitrogen atoms and seven oxygen atoms (DyN₂O₇) provided by one nitrate and two ligands. At 30 K, the space group changes to another polar space group *Pc*. The main difference between the crystal structures of *Pna*₂₁ and *Pc* is the *Z*-value and the ordering of solvent alcohol molecule. As a result, there are two types of molecular structure in the polar *Pc* space group, as shown in Figure 1b. Four different orientation triangular molecules and four ethanol molecules surround the 2₁ screw axis in the *Pna*₂₁ phase but two different orientation triangular molecules and two ethanol molecules in the *Pc* phase which induced different molecular packing. The local coordination symmetry of each Dy³⁺ center was analyzed by continuous shape measure^[21] calculations on the DyO₈ and DyN₂O₇ sites. At both 298 and 30 K, the calculations reveal that Dy1 is situated in a slightly distorted *D*_{4d} geometry while Dy2 and Dy3 are situated within a *C*_{4v} coordination environment with different deviation values.

Based on the determined geometries of the Dy₃ complex at 30 K, Complete-active-space self-consistent field (CASSCF) calculations on individual Dy³⁺ fragments were carried out.

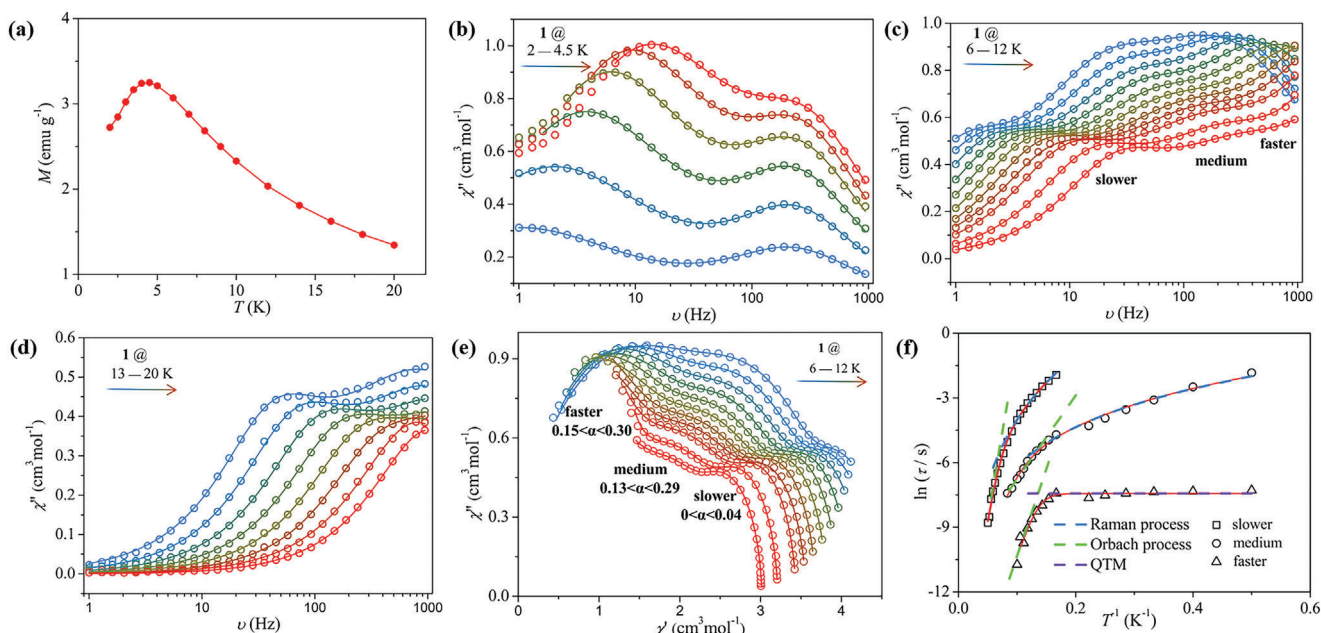


Figure 2. Magnetic relaxation analyses. a) Temperature dependence of magnetization measured in 1000 Oe. b–d) Imaginary component of ac magnetic susceptibility as a function of frequency in different temperature ranges. e) The Cole–Cole plots at 6–12 K show three distinct magnetic relaxation processes, named faster, medium, and slower, respectively. f) The relaxation time $\ln(\tau)$ as a function of the reciprocal of temperature. The different relaxation processes are marked in different symbols. The solid lines are the best fitting results using the sum of three modified Debye functions.

The energy levels, g tensors, and the predominant m_j values of the lowest eight Kramers doublets (KDs) of individual Dy^{3+} fragments were obtained. POLY_ANISO program^[22–25] was used to fit the Dy^{3+} - Dy^{3+} exchange interactions and the intermolecular interactions through comparison of the computed and measured magnetic susceptibilities. The computational details are described in the Supporting Information. The results suggest that the Dy^{3+} - Dy^{3+} interactions in the Dy_3 clusters are antiferromagnetic. The magnetic axes on Dy^{3+} ions in the two molecular structures are indicated in Figure 1b. The included angles between magnetic easy axes of Dy^{3+} ions are all larger than 97° . Therefore, the local magnetization vectors of Dy^{3+} ions can be approximately regarded as a triangle. Subsequently, a toroidal moment is formed based on the Dy_3 magnetic triangles.

A vanishing small magnetic susceptibility at low temperatures would be expected for the state with toroidal magnetic moments, as reported in previous studies.^[20] Figure 2a shows the temperature dependence of dc magnetization of the Dy_3 complex. The magnetization exhibits a maximum of around 4.5 K and decreases toward zero at low temperatures. This feature is consistent with the anticipated behavior of a SMM with toroidal magnetic moments.

The ac magnetic susceptibility of the Dy_3 complex exhibits a strongly frequency-dependent behavior in the temperature range from 2 to 20 K (see Figure S1, Supporting Information), which is another characteristic of SMMs. Especially, the imaginary component (χ'') shows an unusual feature of multiple peaks, indicating multiple magnetic relaxation processes. In the low-temperature region (2–4.5 K), χ'' shows two separate peaks, corresponding to a slow (low frequency) and fast (high frequency) relaxation process, respectively, as shown in Figure 2b. While the slow relaxation shifts to higher frequencies with increasing

temperature, the fast relaxation process is almost temperature-independent, which suggests that the fast relaxation is related to quantum tunneling of magnetization (QTM).^[26] In the intermediate temperature region (6–12 K), three distinguishable relaxation processes, named as the faster, medium, and slower processes, coexist (Figure 2c). Both the slower and medium relaxations shift to higher frequencies as temperature increases. In the high-temperature region, the medium relaxation process gradually shifts to high frequencies and becomes undetectable while the slow relaxation process remains (Figure 2d). The strong shift with the temperature of the slower and medium relaxation processes indicates that they are related to thermally activated processes.

Interestingly, the experimental data between 6 and 12 K can be nicely simulated and depicted as the Cole–Cole plots^[27] which provide a more indicative view of the evolution and coexistence of multiple relaxation processes, as shown in Figure 2e. The relaxation time (τ) for each process can be extracted by fitting the $\chi''(\nu)$ curves to three relaxation processes using the sum of three modified Debye functions,^[28]

$$\chi_{\text{ac}}(\omega) = \chi_{\text{S}} + \sum_k \frac{\Delta\chi_k}{1 + (i\omega\tau)^{(1-\alpha_k)}} \quad (1)$$

$$\chi_{\text{S}} = \sum_k \chi_{\text{S},k}; \Delta\chi_k = \chi_{\text{T},k} - \chi_{\text{S},k}$$

where $\chi_{\text{S}} = \chi_{\text{S}1} + \chi_{\text{S}2} + \chi_{\text{S}3}$ represents the sum of the adiabatic susceptibilities of the three and two relaxing species; $\Delta\chi_k$ is the difference between the adiabatic susceptibility ($\chi_{\text{S},k}$) and the isothermal susceptibility ($\chi_{\text{T},k}$) of each magnetic phase; $\omega = 2\pi\nu$ and the parameter α is the quantifying the width of the τ distri-

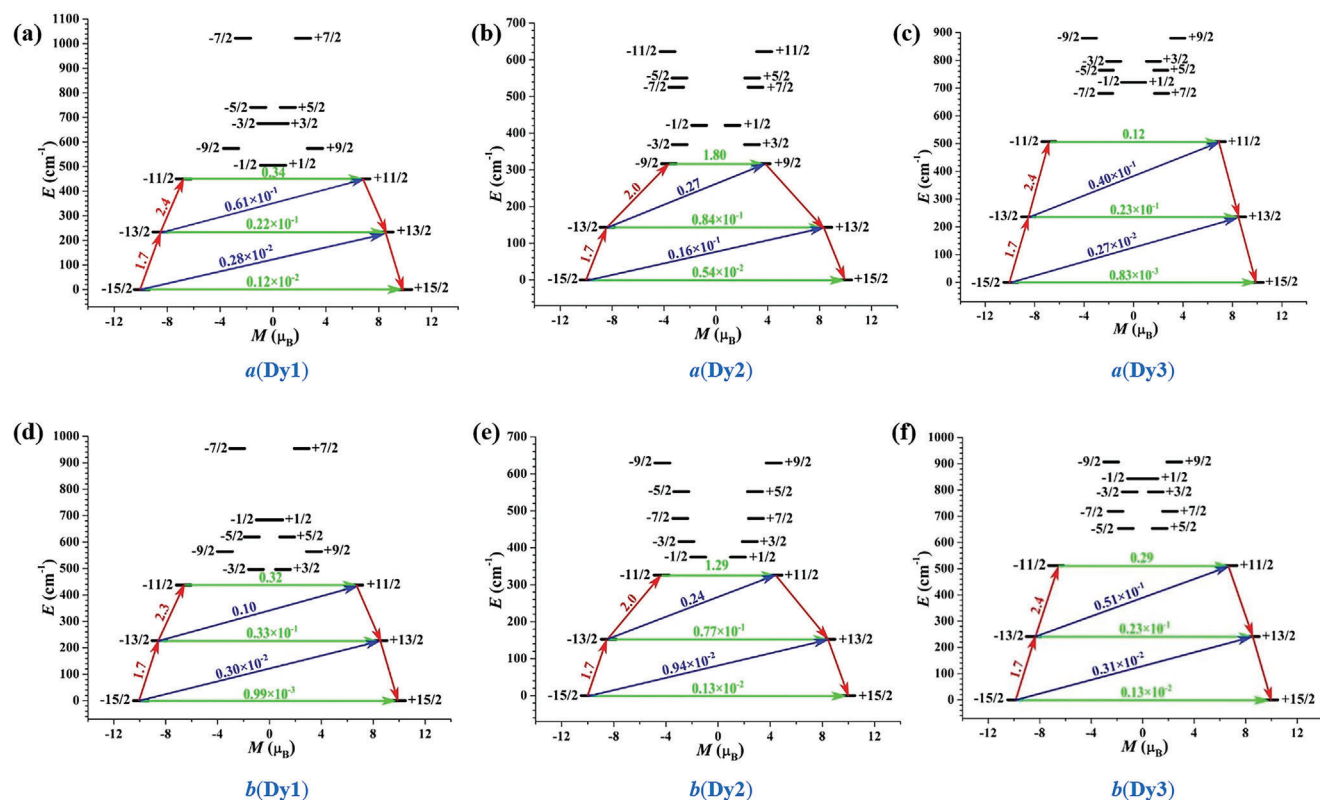


Figure 3. Magnetization blocking barriers of individual Dy^{3+} fragments. The thick black lines represent the KDs as a function of their magnetic moment along the magnetic axis. The green lines correspond to diagonal quantum tunneling of magnetization (QTM); the blue line represents off-diagonal relaxation process. The numbers at each arrow stand for the mean absolute value of the corresponding matrix element of transition magnetic moment.

tribution. The small α values ($\alpha < 0.30$) indicate that each relaxation phase has a very narrow distribution of relaxation times. And the remainder two temperature ranges of 2 to 4.5 K and 13 to 20 K are fitted by the sum of two modified Debye functions with $\chi_S = \chi_{S1} + \chi_{S2}$.

The correlation between the relaxation time (τ) and temperature (T) can be obtained from a plot of $\ln(\tau)$ versus $\ln(T)$ to give n values for the three relaxation processes (n is the parameter that represents the relation between the relaxation time and temperature in the equation $\tau = T^{-n}$). These results indicate that the medium and slow processes are dominated by the Raman process and Orbach relaxation pathways, while QTM dictates the faster process (Figure 2f and Figure S2, Supporting Information).

The corresponding magnetization blocking barriers of individual Dy^{3+} fragments are shown in Figure 3, where the transversal magnetic moments in the ground KDs of individual Dy^{3+} fragments are all smaller than $10^{-2} \mu_B$, and thus the quantum tunneling of magnetization (QTM) in their ground KDs could be suppressed at low temperature. For individual Dy^{3+} fragments of **a** and **b**, the transversal magnetic moments in their first excited KDs are all smaller than $10^{-1} \mu_B$, and thus the relaxation can probably proceed through higher excited KDs. For individual Dy^{3+} fragments of **a** and **b**, the transversal magnetic moments in the second excited KDs are all larger than $10^{-1} \mu_B$, therefore, allowing a fast QTM in their second excited KDs. Hence, the calculated energy barriers of individual Dy^{3+} fragments of them according to the scheme of Figure 3 are 450.0, 316.8, 507.0, 437.1,

326.2, and 512.2 cm^{-1} , respectively. Due to the unfavorable effects of anharmonic phonons, Raman magnetic relaxation, QTM, etc on the energy barrier, the experimental effective U_{eff} are much smaller than the calculated energy gaps between the lowest three KDs of individual Dy^{3+} fragments.

The presence of multiple relaxation channels in SMMs is not unusual, but they usually play a dominating role in different temperature regimes. The coexistence of three relaxation processes at the same temperature has never been observed. Chibotaru et al. concluded that reorientation of the toroidal magnetization requires consecutive transitions through three exchanging excited KDs of Dy3 with the nonmagnetic ground state, whose excitation energies represent the barrier of blockage of this magnetization.^[23] Three exchange excited doublets for each compound are close to each other in Table S7, Supporting Information. Thus, we deduced the coexistence of three relaxation processes at the same temperature may arise from the three near-degenerate exchange excited KDs.

The polar space groups at both high and low temperatures imply that this toroidal SMM could be ferroelectric. We employed the SHG technique to testify intrinsic ferroelectricity in the sample (Figure 4).^[29–31] The relationship between the intensity of the SHG signal from a noncentrosymmetric crystal and its nonlinear polarization is $I_{(2\omega)}/|P_{(2\omega)}|^2$. As shown in Figure 4a, the intensity of the reflection SHG signal of the sample presents a nonlinear variation with incident fundamental optical power, which can be well defined by the quadratic equation, confirming the second

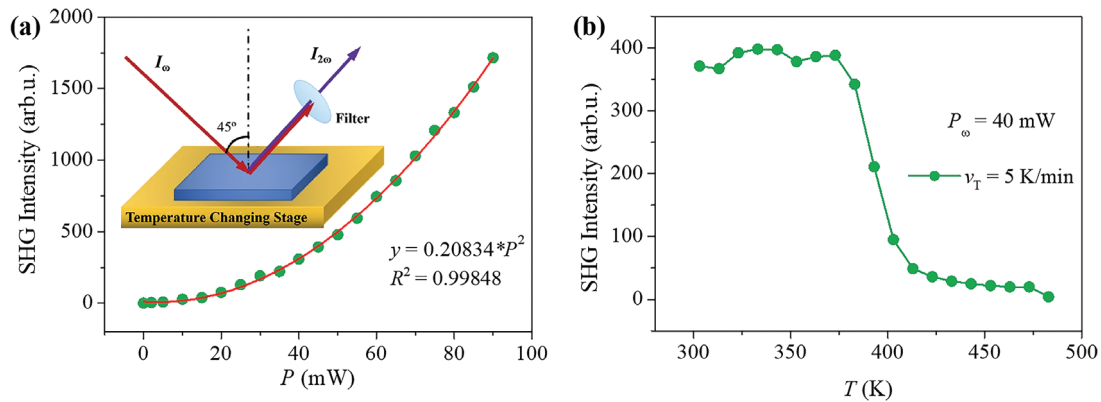


Figure 4. Second nonlinear response. a) Quadratic dependence of the SHG signal as a function of the laser power. As the incident light power increases, the SHG signal increases following the fitting curve $y = A \cdot x^2$ with a high R^2 (Adjusted R Square) value, confirming the second nonlinear response of the nanocrystals. Inset is the Schematic diagram of SHG measurement. The red line is the fitting curve to quadratic dependence. The inset shows the scheme of the SHG measurement. b) SHG intensity as a function of temperature. A ferroelectric phase transition is evidenced by a rapid increase of the intensity around 470 K.

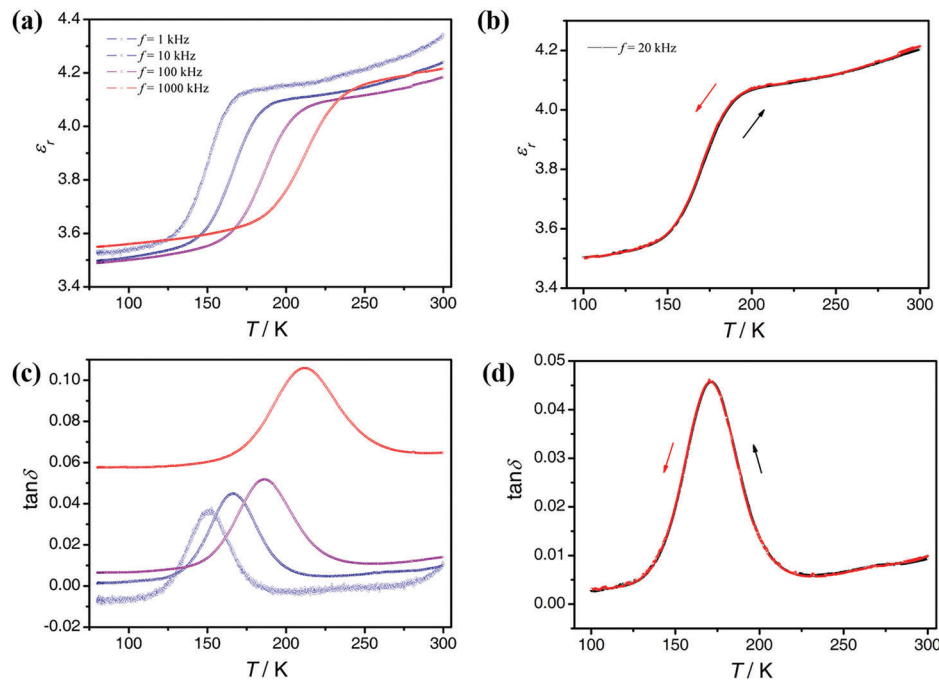


Figure 5. Temperature dependence of a, b) the dielectric permittivity and c, d) loss tangent of the SMM. The dielectric anomaly indicates a ferroelectric-ferroelectric phase transition around 150 K at 1 Hz.

nonlinear response of the nanocrystals. In addition, the SHG signals obtained at high temperatures are almost zero. In contrast, a nonzero SHG signal is visible below ≈ 470 K, which corroborates the emergence of electric polarization and confirms intrinsic ferroelectricity with a Curie temperature above room temperature.

Figure 5 shows the dielectric permittivity (ϵ_r) and loss ($\tan\delta$) as a function of temperature between 80 and 300 K. The sudden rise of ϵ_r , as well as the clear peak in $\tan\delta$ indicate that there is another phase transition around 150 K. Moreover, the SHG intensity abruptly decreases to a minimum but nonzero value of around 150 K (see Figure S6, Supporting Information). The sharp decline in the SHG signal is likely due to the space group change

from $Pna2_1$ to Pc . Since both space groups are polar, this transition around 150 K corresponds to a ferroelectric-ferroelectric phase transition.

3. Conclusion

In summary, our study verifies a unique Dy_3 SMM with toroidal magnetic moments and ferroelectricity, where the local magnetization vectors of Dy^{3+} ions form a triangle and the ferroelectricity is introduced by polar alcohol molecules. Interestingly, three distinct magnetic relaxation processes, corresponding to the Raman, Orbach, and QTM relaxation pathways, respectively, can coexist

in the same temperature range. Hence, a modified Debye model with three relaxation times was introduced to study the multiple dynamic mechanisms. The ferroelectricity with the Curie temperatures $T_C \approx 470$ K was evidenced by the SHG signal that is only allowed in noncentrosymmetric structures. Moreover, the dielectric anomaly around 150 K (1 Hz) suggests a ferroelectric-to-ferroelectric phase transition originated from the symmetry change from Pc to $Pna2_1$. A significantly enhanced ME coupling would be expected in polar SMMs. This could pave the way for the design of molecular multiferroics and magnetoelectric materials using ferroelectric SMMs in the near future. The successful incorporation of ferroelectricity into SMMs not only broadens the family of multiferroics but also opens more opportunities for the electrical control of quantum magnetism of SMMs.

4. Experimental Section

The SMM in this study was a trinuclear (Dy_3) complex with a formula of $[Dy_3(HL)(H_2L)(NO_3)_4] \cdot C_2H_5OH$. The samples were synthesized by a solution method.^[20] $Dy(NO_3)_3 \cdot 6H_2O$ (0.5 mmol, 228.3 mg) was slowly added to a 20 mL isopropanol solution containing H_4L (1.0 mmol, 273 mg) and $LiOH$ (0.4 mmol, 16.8 mg). The mixture was moved to a vial after 2 h of stirring. Colorless crystals were obtained under 100 °C solvothermal condition three days later in a 46% yield (based on Dy). Single-crystal X-ray diffraction was performed on an Agilent SuperNova diffractometer (298 K) and a Bruker D8 Venture diffractometer (30 K) equipped with graphite monochromated Mo-K α radiation ($\lambda = 0.71073$ Å). The structures were solved by direct methods and refined by the full-matrix least-squares method on F^2 with anisotropic thermal parameters for all nonhydrogen atoms using the SHELXL program. Hydrogen atoms were located geometrically and refined isotropically (see Table S1, Supporting Information). Powder X-ray diffraction patterns were measured on a Rigaku Ultima IV diffractometer using Cu-K α radiation (shown in Figure S7, Supporting Information). Magnetic properties were measured on powder samples using a Quantum Design superconducting quantum interference device magnetometer. The dielectric permittivity was measured on a palate made of pressed powder samples with an Aglient 4980A LCR meter in a cryogen-free superconducting magnet system (Oxford Instruments, Teslatron PT). The optical second harmonic generation (SHG) measurements were performed by using a mode-lock femtosecond (fs) Ti:sapphire oscillator (Tsunami 3941-X1BB, Spectra-Physics), which generates the incident fundamental laser with a central wavelength at 800 nm, a pulse duration of ≈ 100 fs, and a repetition rate of 82 MHz. The energy of the incident light was attenuated to 40 mW before being focused. A 400 nm filter was used in the reflective light path to ensure that only SH photons arrived at the photomultiplier tube. A single-photon counting technique was conducted to count the SH photons, indicating the intensity of SHG signals generated from the samples. CASSCF calculations on individual Dy^{3+} fragments of trinuclear complex based on X-ray determined geometries at 30 K have been carried out with MOLCAS 8.4 and SINGLE_ANISO programs.

Supporting Information

Supporting Information is available from the Wiley Online Library or from the author.

Acknowledgements

Financial support for this project was partially provided by the National Key R&D Program of China (grant ref: 2018YFA0306002), the National Natural Science Foundation of China (grant refs: 51725104, 21931004, 21973049, and 21973046), the Ministry of Education of China (grant

ref: B12015), the China Postdoctoral Science Foundation funded project (Grant No. 2019M651009), the Beijing Natural Science Foundation (Grant No. Z180009) and Frontiers Science Center for New Organic Matter, Nankai University (Grant No. 63181206). The authors genuinely appreciated the preliminary dialectical measurements and suggestions of the deceased Prof. James F. Scott and Dr. Jonathan Gardner from St. Andrews University.

Conflict of Interest

The authors declare no conflict of interest.

Data Availability Statement

The data that support the findings of this study are available from the corresponding author upon reasonable request.

Keywords

multiferroic materials, second-harmonic generation, single-molecule magnets, toroidal magnetic moments

Received: May 20, 2022
Revised: June 13, 2022
Published online: July 20, 2022

- [1] W. Wernsdorfer, R. Sessoli, *Science* **1994**, 284, 133.
- [2] D. N. Woodruff, R. E. P. Winpeeny, R. A. Layfield, *Chem. Rev.* **2013**, 113, 5110.
- [3] S. T. Liddle, J. V. Slagereen, *Chem. Soc. Rev.* **2015**, 44, 6655.
- [4] Y.-X. Wang, Y. Ma, Y. Chai, W. Shi, Y. Sun, P. Cheng, *J. Am. Chem. Soc.* **2018**, 140, 7795.
- [5] F. Paschke, T. Birk, V. Enekel, F. Liu, V. Romankov, J. Dreiser, A. A. Popov, M. Fonin, *Adv. Mater.* **2021**, 33, 2102844.
- [6] L. Ungur, S.-Y. Lin, J. Tang, L. F. Chibotaru, *Chem. Soc. Rev.* **2014**, 43, 6894.
- [7] J. Tang, I. Hewitt, N. T. Madhu, G. Chastanet, W. Wernsdorfer, C. E. Anson, C. Benelli, R. Sessoli, A. K. Powell, *Angew. Chem., Int. Ed.* **2006**, 45, 1729.
- [8] B. B. V. Aken, J.-P. Rivera, H. Schmid, M. Fiebig, *Nature* **2007**, 449, 702.
- [9] W. Jin, E. Drueke, S. Li, A. Admasu, R. Owen, M. Day, K. Sun, S.-W. Cheong, L. Zhao, *Nat. Phys.* **2020**, 16, 42.
- [10] L. Ungur, S. K. Langley, T. N. Hooper, B. Moubaraki, E. K. Brechin, K. S. Murray, L. F. Chibotaru, *J. Am. Chem. Soc.* **2020**, 134, 18554.
- [11] S. Xue, X.-H. Chen, L. Zhao, Y.-N. Guo, J. Tang, *Inorg. Chem.* **2012**, 51, 13264.
- [12] S.-Y. Lin, W. Wernsdorfer, L. Ungur, A. K. Powell, Y.-N. Guo, J. Tang, L. Zhao, L. F. Chibotaru, *Angew. Chem., Int. Ed.* **2012**, 51, 12767.
- [13] J. Luzon, K. Bernot, I. J. Hewitt, C. E. Anson, A. K. Powell, R. Sessoli, *Phys. Rev. Lett.* **2008**, 100, 247205.
- [14] X.-L. Liu, D. Li, H.-X. Zhao, X.-W. Dong, L.-S. Long, L.-S. Zheng, *Adv. Mater.* **2021**, 33, 2004542.
- [15] L. Bogani, W. Wernsdorfer, *Nat. Mater.* **2008**, 7, 179.
- [16] M. Mannini, F. Pineider, C. Danieli, F. Totti, L. Sorace, P. H. Sainctavit, M.-A. Arrio, E. Otero, L. Joly, J. C. Cezar, A. Cornia, R. Sessoli, *Nature* **2010**, 468, 417.
- [17] M. Fiebig, T. Lottermoser, D. Meier, M. Trassin, *Nat. Rev. Mater.* **2006**, 1, 16046.
- [18] L. C. Gómez-Aguirre, B. Pato-Doldán, J. Mira, S. Castro-García, M. A. Señarís-Rodríguez, M. Sanchez-Andújar, J. Singleton, V. S. Zapf, *J. Am. Chem. Soc.* **2016**, 138, 1122.

- [19] Y. Tian, W. Wang, Y. Chai, J. Cong, S. Shen, L. Yan, S. Wang, X. Han, Y. Sun, *Phys. Rev. Lett.* **2014**, *112*, 017202.
- [20] Y.-X. Wang, W. Shi, H. Li, Y. Song, L. Fang, Y. Lan, A. K. Powell, W. Wernsdorfer, L. Ungur, L. F. Chibotaru, M. Shen, P. Cheng, *Chem. Sci.* **2012**, *3*, 3366.
- [21] S. Alvarez, P. Alemany, D. Casanova, J. Cirera, M. Llunell, D. Avnir, *Coord. Chem. Rev.* **2005**, *249*, 1693.
- [22] F. Aquilante, J. Autschbach, R. K. Carlson, L. F. Chibotaru, M. G. Delcey, L. De Vico, I. F. Galván, N. Ferré, L. M. Frutos, L. Gagliardi, M. Garavelli, A. Giussani, C. E. Hoyer, G. L. Manni, H. Lischka, D. Ma, P. Å. Malmqvist, T. Müller, A. Nenov, M. Olivucci, T. B. Pedersen, D. Peng, F. Plasser, B. Pritchard, M. Reiher, I. Rivalta, I. Schapiro, J. Segarra-Martí, M. Stenrup, D. G. Truhlar, et al., *J. Comput. Chem.* **2016**, *37*, 506.
- [23] L. F. Chibotaru, L. Ungur, A. Soncini, *Angew. Chem., Int. Ed.* **2008**, *47*, 4126.
- [24] L. Ungur, W. Van den Heuvel, L. F. Chibotaru, *New J. Chem.* **2009**, *33*, 1224.
- [25] L. F. Chibotaru, L. Ungur, C. Aronica, H. Elmoll, G. Pilet, D. Luneau, *J. Am. Chem. Soc.* **2008**, *130*, 12445.
- [26] M. A. Novak, W. S. D. Folly, J. P. Sinnecker, S. Soriano, *J. Magn. Magn. Mater.* **2005**, *294*, 133.
- [27] K. S. Cole, R. H. Cole, *J. Chem. Phys.* **1941**, *9*, 341.
- [28] Y.-N. Guo, G.-F. Xu, W. Wernsdorfer, L. Ungur, Y. Guo, J. Tang, H.-J. Zhang, L. F. Chibotaru, A. K. Powell, *J. Am. Chem. Soc.* **2011**, *133*, 11948.
- [29] B. Zalar, V. V. Laguta, R. Blinc, *Phys. Rev. Lett.* **2003**, *90*, 037601.
- [30] X. Feng, Y. Lun, X. Jiang, J. Qiu, H. Yu, S. Zhou, *Adv. Mater* **2021**, *33*, 2006482.
- [31] A. M. Pugachev, V. I. Kovalevskii, N. V. Surovtsev, S. Kojima, S. A. Prosandeev, I. P. Raevski, S. I. Raevskaya, *Phys. Rev. Lett.* **2012**, *108*, 247601.